

# Chemical Species Separation with Simultaneous Estimation of Field Map and $T_2^*$ Using a $k$ -Space Formulation

Jose Luis Honorato,<sup>1,2</sup> Vicente Parot,<sup>1,2</sup> Cristian Tejos,<sup>1,2</sup> Sergio Uribe,<sup>2,3</sup> and Pablo Irarrazaval<sup>1,2\*</sup>

**Chemical species separation techniques in image space are prone to incorporate several distortions. Some of these are signal accentuation in borders and geometrical warping from field inhomogeneity. These errors come from neglecting intraecho time variations. In this work, we present a new approach for chemical species separation in MRI with simultaneous estimation of field map and  $T_2^*$  decay, formulated entirely in  $k$ -space. In this approach, the time map is used to model the phase accrual from off-resonance precession and also the amplitude decay due to  $T_2^*$ . Our technique fits the signal model directly in  $k$ -space with the acquired data minimizing the  $l_2$ -norm with an interior-point algorithm. Standard two dimensional gradient echo sequences in the thighs and head were used for demonstrating the technique. With this approach, we were able to obtain excellent estimation for the species, the field inhomogeneity, and  $T_2^*$  decay images. The results do not suffer from geometric distortions derived from the chemical shift or the field inhomogeneity. Importantly, as the  $T_2^*$  map is well positioned, the species signal in borders is correctly estimated. Considering intraecho time variations in a complete signal model in  $k$ -space for separating species yields superior estimation of the variables of interest when compared to existing methods. Magn Reson Med 000:000–000, 2011. © 2011 Wiley Periodicals, Inc.**

**Key words:** magnetic resonance imaging; chemical species separation; fat and water; field inhomogeneities; off-resonance correction;  $T_2^*$  map

Separation of chemical species from MR images is useful for assistance in patient diagnosis (1). For example, discrimination of fat from water in the liver allows non-invasive fat quantification and fat fraction determination. The prominent signal brightness and spatial displacement of fat in some imaging studies can interfere with the diagnosis of pathologies, where reliable fat suppression proves to be difficult (2). Most fat–water separation techniques take advantage of the chemical shift between these species,

which makes fat spins precess slower than water spins. This causes a displacement of the fat signal in the readout direction and signal cancellation in out of phase images. Since the original two-point Dixon approach (3), fat–water separation techniques have been considerably improved with new methods, such as three-point (4) and multipoint Dixon (5), extended two-point Dixon (6–8), and iterative decomposition of water and fat with echo asymmetry and least-squares estimation (IDEAL) (9,10), all of them successfully used for fat quantification (11). Multispecies separation is also possible with some of these approaches. Extended two-point Dixon and IDEAL incorporate the field inhomogeneity in their signal models, obtaining superior results compared to other techniques, which usually neglect this variable. Strong field inhomogeneities can distort species separation, and so several phase unwrapping algorithms have been proposed to correct these distortions (12,13).

To obtain a better estimation of fat and water, the MR signal model should also take into account the effective transverse relaxation time ( $T_2^*$ ) or rate ( $R_2^* = 1/T_2^*$ ) of the species and the multipoint spectrum model of fat. If the  $R_2^*$  for water and fat are not included in the reconstructed images, an erroneous estimation of the fat fraction can occur (14–17). The  $R_2^*$  parameter can be incorporated in the signal model, yielding a more accurate calculation of the fat fraction (1,17–20). Considering different decay rates for fat and water also improves the quantification of both species (17). Additionally, the MR spectrum of fat usually presents intersubject variability (15,21). For example, the hepatic lipid concentration in the liver of different patients diagnosed with steatosis may differ significantly from that of healthy subjects (21). Traditionally, fat has been represented as a single peak 3.5 ppm away from the water peak. This allows a simple formulation of the signal, enabling an easily tractable framework for the theories used in fat suppression and saturation methods and Dixon-like methods. However, representing fat as a sum of several peaks located at different positions of the spectrum, weighed by the corresponding fraction of each peak, leads to a more accurate estimation of the fat fraction. It also allows the visualization of certain structures that can remain hidden when using a single peak approach (22,23).

All the previous methods separate the species in image space, after the application of an inverse Fourier transform of  $k$ -space data. These schemes assume that the acquisition happens instantaneously at the echo time (TE). This assumption produces some image distortions due to

<sup>1</sup>Department of Electrical Engineering, Pontificia Universidad Catolica de Chile, Santiago, Chile

<sup>2</sup>Biomedical Imaging Center, Pontificia Universidad Catolica de Chile, Santiago, Chile

<sup>3</sup>Department of Radiology, Pontificia Universidad Catolica de Chile, Santiago, Chile

Grant sponsor: CONICYT; Grant numbers: FONDECYT 1070674, 1100529, ANILLO PBCT-ACT-79

\*Correspondence to: P. Irarrazaval, Ph.D., Ingenieria Electrica, Pontificia Universidad Catolica de Chile, Av. Vicuna Mackenna 4860, 7820436 Macul, Santiago, Chile. E-mail: pim@ing.puc.cl

Received 6 July 2011; revised 1 September 2011; accepted 8 September 2011.

DOI 10.1002/mrm.23237

Published online in Wiley Online Library (wileyonlinelibrary.com).

© 2011 Wiley Periodicals, Inc.

phase accumulation from off-resonance frequencies during the readout. This off-resonance deviation is caused by the combination of the species resonance frequency and the local field inhomogeneity. In some approaches, field inhomogeneity is corrected a posteriori (24). Using a model based in a  $k$ -space formulation of the acquired signal that acknowledges the phase accumulation of off-resonance spins during the readout process leads to improvements, such as correction of chemical shift displacements or blurring. Brodsky et al. (25) used a variable time map that successfully corrects chemical shift-related artifacts. A more complete signal model is presented in Ref. 20, where each pixel is modeled with a single  $R_2^*$  rate, generating a  $R_2^*$  map for the entire object. In both  $k$ -space decomposition method, the field and  $R_2^*$  maps are obtained in the image domain and then demodulated from the acquisitions. Unfortunately, image-space displacement caused by field inhomogeneity is difficult to correct using this approach. Additionally, when using low bandwidth acquisitions with Cartesian  $k$ -space trajectories where fat–water overlap may occur, a displaced estimation of the  $R_2^*$  decay is obtained, leading to an erroneous estimation of the species intensity.

In this work, we propose a new method for field inhomogeneity,  $R_2^*$ , and species estimation using a variable time map (FIRST). Unlike current methods, FIRST accounts for the phase accumulation due to field inhomogeneity and for the signal decay during the readout. Thus, it is able to correct the artifacts caused by chemical shift and field inhomogeneity. Moreover, the  $R_2^*$  map is calculated in the undisplaced positions. The estimation is achieved by minimizing the difference between the acquired signal and an accurate signal model of each  $k$ -space position. An interior-point algorithm was used to solve the minimization problem. Estimates for the unknowns are generated directly in image space. Similar to previous methods, it does not need specific TE combinations, allowing the use of short TE sequences, and a multipoint signal model can be introduced for superior fat estimation.

## THEORY

### Review of IDEAL-Like Techniques

The IDEAL algorithm (9,10) is an iterative method for achieving accurate separation of chemical species. As an extension of the multipoint Dixon technique, IDEAL can obtain separate images for  $M$  species with the acquisition of at least  $M + 1$  images at different TEs. The image quality will depend on the chosen TEs (26), which are not restricted to specific phase shifts as in Dixon-like methods. Therefore, IDEAL is very useful for combining water–fat separation capabilities with short TE and pulse repetition time. The signal model used in IDEAL for one pixel at location  $\mathbf{r}$  containing  $M$  species with chemical shifts  $\Delta f_m$  (Hz) ( $m = 1, \dots, M$ ) acquired during echo  $n$  at a discrete echo time  $t_n$  is the following,

$$s_n(\mathbf{r}) = \left( \sum_{m=1}^M \rho_m(\mathbf{r}) e^{i2\pi\Delta f_m t_n} \right) e^{i2\pi\psi(\mathbf{r})t_n}$$

with  $\rho_m(\mathbf{r})$  the complex intensity of the  $m$ th species and  $\psi(\mathbf{r})$  the local magnetic resonance offset (Hz). If  $s_n^a(\mathbf{r})$  represents the acquired signal for all species in location  $\mathbf{r}$ , then the minimization functional of IDEAL for a set of pixels in position  $\mathbf{r}$  is as follows,

$$\min_{\substack{\rho_m(\mathbf{r}) \in \mathbb{C} \\ \psi(\mathbf{r}) \in \mathbb{R}}} \left\| s_n^a(\mathbf{r}) - \sum_{m=1}^M \rho_m(\mathbf{r}) e^{i2\pi(\Delta f_m + \psi(\mathbf{r})) \cdot t_n} \right\|_2.$$

This minimization is performed separately for each pixel and is implemented such that the current estimated field map is used to demodulate the acquired values. The resultant signal after demodulation is therefore

$$\hat{s}_n(\mathbf{r}) = s_n(\mathbf{r}) e^{-i2\pi\psi(\mathbf{r})t_n} = \sum_{m=1}^M \rho_m(\mathbf{r}) e^{i2\pi\Delta f_m t_n}.$$

After a linearization of the exponential term, a new estimate for the field map and species can be obtained with least squares, until the field map converges.

In the work of Brodsky et al. (25), the true time of the acquisition is given for each echo, allowing the correction of chemical shift-based displacement of species. If the time map is considered in the signal model, the inverse Fourier transform of  $\hat{s}_n(\mathbf{r})$  is  $\hat{S}_n(\mathbf{k})$  described by

$$\hat{S}_n(\mathbf{k}) = \sum_{m=1}^M R_m(\mathbf{k}) e^{i2\pi\Delta f_m(t_n + \tau_{\mathbf{k},n})}$$

where  $R_m(\mathbf{k})$  are the Fourier transform of the species,  $t_n$  is the nominal echo time and  $\tau_{\mathbf{k},n}$  is the relative time between the acquisition of sample point  $\mathbf{k}$  and the center of  $k$ -space. Using a similar decomposition method as in conventional IDEAL, the Fourier values for each species are obtained, leading to nonshifted estimates of fat and water. Nevertheless, the field map is demodulated in image space, as if it were acquired with a fixed time map. For this reason, displacements caused by field inhomogeneity are not corrected, whose implications are described later. We denote these methods as image-space decomposition methods, as, while spectral decomposition occurs in  $k$ -space, the field and  $R_2^*$  maps are demodulated in image space. This is equivalent to assuming a fixed time map as an approximation to the true time map, which is not constant.

### FIRST Signal Model

Considering a  $k$ -space trajectory given by  $k(t)$ , the estimated MR signal for an object containing  $M$  different species is given by

$$S^e(t) = \sum_{m=1}^M \int \rho_m(\mathbf{r}) e^{-i2\pi[\mathbf{r} \cdot k(t) + (\Delta f_m + \psi(\mathbf{r})) \cdot t]} d\mathbf{r}.$$

This signal model takes into account a variable time map for the chemical shift of each species and the field map intensities for each position. For a single species  $m$ , the discrete version of the estimated signal  $S_{mq}^e(t)$  is given by

$$S_{mq}^e = \sum_{\mathbf{r}} \rho_{m,\mathbf{r}} e^{-i2\pi(\Delta f_m + \psi_{\mathbf{r}}) \cdot q} e^{-i2\pi\mathbf{r} \cdot \mathbf{k}_q}$$

where  $\mathbf{r}$  is the discrete position of spin densities and  $q$  is the time at which sample  $k_q$  was acquired. The purpose is to adjust the unknown variables of the estimated model ( $\rho_m$  and  $\psi$ ) to the values of the acquired signal. If  $S_q^a$  is the acquired signal for all species at a specific time  $q$ , the reconstruction functional is

$$\min_{\substack{\rho_m \in \mathbb{C}^N \\ \psi \in \mathbb{R}^N}} \left\| S_q^a - \sum_{m=1}^M \sum_{\mathbf{r}} \rho_{m,\mathbf{r}} e^{-i2\pi(\Delta f_m + \psi_{\mathbf{r}}) \cdot q} e^{-i2\pi \mathbf{r} k_q} \right\|_2. \quad [1]$$

In this minimization, there are  $2M + 1$  scalar unknowns of length  $N$  ( $M$  is the number of species and  $N$  the number of acquired points). Each acquisition adds  $2N$  equations to the system. It is necessary to acquire  $M + 1$  times to have a complete set of equations and unknowns. Therefore, our method does not increase the amount of data needed for species separation when compared to similar decomposition methods. The objective function is similar to the one in Ref. 13, with the difference that in this model a variable time map is introduced. In the following section, we will describe a more complete signal model that takes into account the  $T_2^*$  decay of the signal. In the discussion, we will refer to multipoint fat spectrum. The extension for 2D Cartesian acquisitions can be found in Appendix A.

### $T_2^*$ Decay

The previous formulations do not consider the  $T_2^*$  decay of the MR signal. Correcting the species intensities from their  $T_2^*$  decay produces better results, specially for those species with short  $T_2^*$  times (17). In Ref. 19, the signal model assumes the same  $T_2^*$  value for every species if they coexist in a single voxel. For that approach, they introduced a new notation where the field map is complex and denoted by  $\tilde{\psi}(\mathbf{r}) = \psi(\mathbf{r}) + iR_2^*(\mathbf{r})/2\pi$ . For image-space decomposition algorithms, the complex field map is demodulated from the acquired signal in image space. Considering a fixed time map for the complex field map may lead to some distortions. For example, if cartesian imaging is used, species estimates are erroneously  $R_2^*$ -corrected in fat–water overlapping regions. This case can be typically found in low-bandwidth acquisitions. Similar examples can be encountered for other trajectories. Moreover, acquisitions with different bandwidths (and different off-resonance artifacts) would produce severely erroneous field and  $R_2^*$  maps, that will affect the separation of species when demodulating the maps in image space before the separation process.

When considering a variable time map, the signal decay at each sampling time can be corrected, which is not possible to do if a fixed time map for the complex field map is considered. In our model, we will consider a single  $R_2^*$  parameter for all species within a pixel. It is important to note that the MR signal depends on the acquisition time, so the exponential decay must depend on the time map  $t$  rather than TE only. Then the discrete minimization functional is

$$\min_{\substack{\rho_m \in \mathbb{C}^N \\ \psi \in \mathbb{R}^N}} \left\| S_q^a - \sum_{m=1}^M \sum_{\mathbf{r}} \rho_{m,\mathbf{r}} \cdot e^{-i2\pi(\Delta f_m + \tilde{\psi}_{\mathbf{r}}) \cdot q} \cdot e^{-i2\pi \mathbf{r} k_q} \right\|_2.$$

The minimization of this functional yields  $\rho_m(x)$ ,  $\psi(x)$ , and  $R_2^*(x)$  in their nondisplaced positions. In this case,  $2M + 2$  acquisitions are needed to obtain the estimates. In our formulation, the  $\tilde{\psi}$  term is multiplied by the time map of the acquisition, so the signal decay during the readout is considered.

## MATERIALS AND METHODS

### MRI Acquisitions

A conventional 2D gradient echo sequence with Cartesian trajectories was performed in the thigh and brain of two healthy subjects. Institutional Review Board approval and informed consent were obtained from volunteers prior to imaging. All images were obtained using a Philips Intera 1.5 T scanner (Philips Healthcare, Best, The Netherlands). For thigh imaging, a four-element body coil was used, and four acquisitions were obtained with the following parameters: matrix size  $256 \times 256$ , TE = 4.6, 4.8, 6.2, 7.5 ms, flip angle =  $25^\circ$ , slice thickness = 10 mm, pulse repetition time = 150 ms, field of view = 18 cm with sampling bandwidth of  $\pm 13.8$  kHz (217 Hz/pixel), scan time = 152 s. For brain imaging, a quadrature head coil was used, with the same sequence parameters except for field of view = 25.6 cm. Pulse repetition time and TE were arbitrarily chosen to achieve similar signal intensities from fat and water, while maintaining a short scan time. Any other echo combinations can be used, but adequate spacing should be considered to reduce noise (26) and to obtain a better  $T_2^*$  exponential fitting. Automatic shimming procedures were not performed in any of the scans. To maximize resolution, no windowing or filtering was applied to the input data. For each dataset, complex echo images were processed to obtain estimates of fat and water with FIRST and IDEAL algorithms. The water–fat frequency shift was assumed to be  $-3.5$  ppm, or  $-217.1$  Hz at 1.5 T. Magnitude images for fat, water, and in-phase combination (water plus fat) were generated in addition to field and  $R_2^*$  maps. Finally, to demonstrate the performance of FIRST throughout hard water–fat transitions and high fat fraction scenarios, we performed a phantom study. Using a home-made phantom consisting of a bottle filled with water with an additional oil tube in its center, similar acquisitions as in vivo studies were performed. The parameters were TE = 4.6, 5.2, 5.5, 5.9, 6.3, 7.0 ms, matrix size  $128 \times 128$  pixels, with the remaining parameters similar to the ones previously outlined. Afterward, fat and water were separated using FIRST and IDEAL.

### IDEAL Algorithm

An implementation of the  $T_2^*$ -IDEAL algorithm (19) was written in MATLAB 7.4 (The MathWorks Inc., Natick, MA). We first performed a standard IDEAL decomposition (9). The resulting species and field map were used as a starting point for calculating the complex field map and the corrected species for  $T_2^*$ -IDEAL, as suggested in Ref. 19. The ranges for field inhomogeneity and  $R_2^*$  were set to  $-150$  to  $150$  Hz and  $0$  to  $350$  s $^{-1}$ , respectively. Even though field inhomogeneity is usually set in the range  $[-\Delta f_{\text{fat}}/2, \Delta f_{\text{fat}}/2]$  (13), we decided to broaden these limits to avoid phase wraps. For each pixel, an update of less than  $10^{-2}$  Hz for the field map and  $10^{-4}$  s $^{-1}$  for  $R_2^*$  were used as the stopping

condition. A maximum of 200 iterations were executed for both IDEAL and  $T_2^*$ -IDEAL if these tolerances were not reached. Before calculating the final estimate of species, the field map was filtered with a gaussian filter of size  $3 \times 3$  and  $\sigma = 1.5$  to achieve better water-fat separation. The processing time for a set of four acquisitions of size  $256 \times 256$  pixels was 9 min. From now on, we will refer to  $T_2^*$ -IDEAL simply as IDEAL.

### FIRST Algorithm

Our proposed technique requires an optimization algorithm suitable for a nonlinear objective function with linear constraints. We used the interior-point algorithm (27,28) available in the `fmincon` function of MATLAB's Optimization Toolbox. The interior-point method was chosen for being stable and faster than other available options, such as trust-region reflective, active set, and Sequential Quadratic Programming (SQP). Upper and lower bounds are provided for all variables. For each pixel of the species, a maximum absolute value is defined as 1.5 times the maximum absolute value available in all acquisitions. This maximum value is used as the upper bound for the real and imaginary parts of every species. The negative of the maximum value is used for the lower bound. The ranges for field inhomogeneity and  $R_2^*$  were the same as in IDEAL. There are no additional constraints for the variables, although they could be used to assure certain smoothness of the field and  $R_2^*$  map.

The final implementation of the algorithm consisted of two steps. The first step consists of estimating the species and the field map without considering  $R_2^*$  decay. In the second step, we re-estimate the species and the field map but now calculating a  $R_2^*$  map (with a single  $R_2^*$  value per pixel). The estimates for the species and field map are used as the starting point of the second step. A flowchart of the optimization process is shown in figure 1. The proposed minimization problem is a nonlinear and nonconvex problem. Because of the periodic nature of the complex exponential terms in the MR signal model described in the objective function, the global minima can be obtained through multiple solutions. This issue will be addressed later in the Discussion section. Bounds for all variables were provided, creating a convex feasible set. Even for this complicated objective function, the algorithm proved to be useful at estimating the unknown variables. Explicitly calculated gradients were supplied for speed improvements, which can be found in Appendix B. The objective value and the gradients of the objective function were calculated with an auxiliary function written in C and compiled with Microsoft Visual C++ 2010. Three different stopping criteria were used for each step of the algorithm: a step size norm lower than  $10^{-9}$  or a maximum of 280 iterations or an objective function lower than  $10^{-7}$ , whichever was reached first. These values were chosen experimentally and applied for both steps of the estimation process. The processing time for a set of four acquisitions of size  $256 \times 256$  pixels was 71 min.

To speed up the convergence of IDEAL and FIRST, an initial estimate for the  $R_2^*$  map was generated. The initial value of  $R_2^*$  for each pixel was calculated by fitting a single exponential function to the absolute values of each

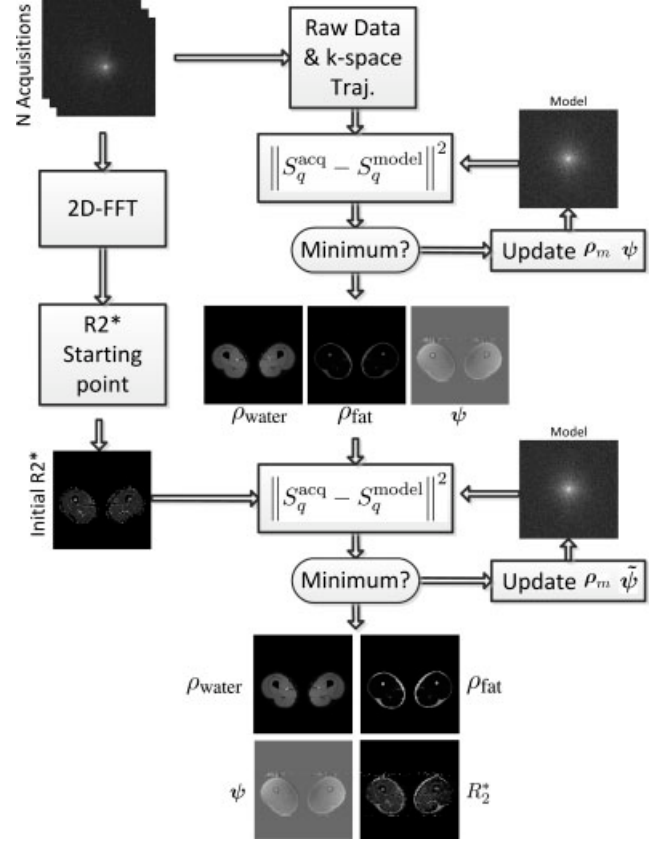


FIG. 1. Flowchart of our implementation for solving the optimization problem. It considers a two-step minimization. The first step consists of estimating the complex value of the chemical species ( $\rho_{\text{water}}$ ,  $\rho_{\text{fat}}$ ) and field map ( $\psi$ ). When these variables are calculated, they are used as an input for the second step, which calculates the  $R_2^*$  and field maps and re-estimates species. We used a starting point for  $R_2^*$  based on an exponential fitting of the signal decay.

acquisition. Values outside the  $0\text{--}350\text{ s}^{-1}$  range were saturated to these bounds. These are within the normal range even for subjects with very high iron deposition (18,20,29). After calculating the value for each pixel in the image, a mask was applied to eliminate the values outside the object. Finally, the result was smoothed with a gaussian filter of size  $5 \times 5$  and  $\sigma = 1$ . This procedure only adds 34.4 s. All computations were performed in a computer with an Intel i7 processor (4 cores, 3.4 GHz, 64-bit) with 8 GB of RAM.

### RESULTS

The results for FIRST and IDEAL when processing gradient echo images of the thigh are shown in Figs. 2–4. Images for absolute values of water, fat, water plus fat, field inhomogeneity and  $R_2^*$  are presented. Water plus fat images were obtained by adding the complex values of water and fat, followed by taking the absolute value of the result. FIRST provides better results for the species in regions with water-fat overlap, mainly because the  $R_2^*$  decay is well positioned compared to the map generated with IDEAL. The voxel size for this acquisition was  $4.94\text{ mm}^3$ , which notably increases the noise level of the input images. Noisy input images were chosen to analyze the behavior of FIRST under these conditions. This makes exponential fitting for

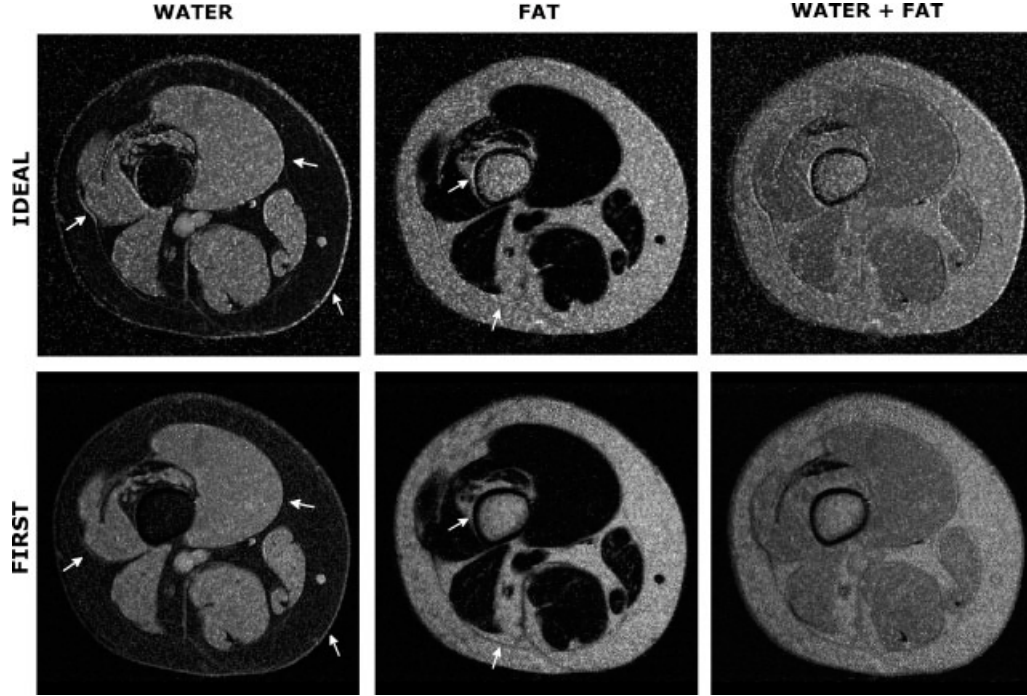
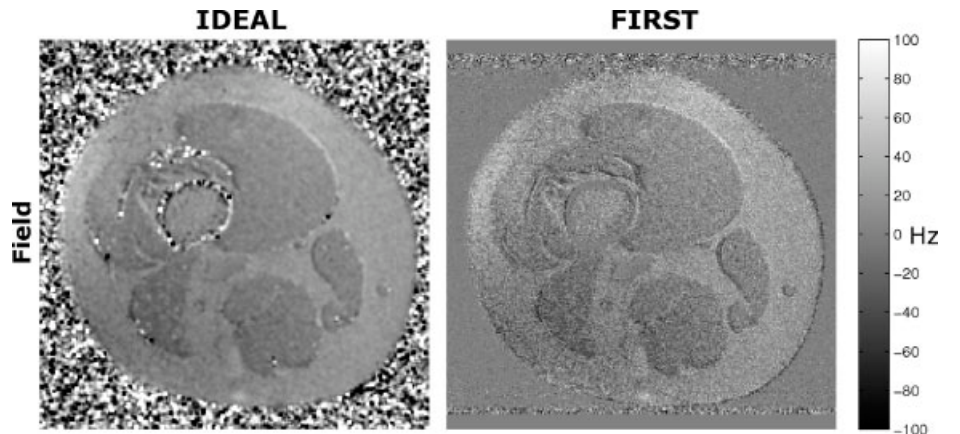


FIG. 2. Magnitude images of water, fat and complex sum of both components for the thigh. The upper and lower rows show the results for IDEAL and FIRST, respectively. The arrows show areas where notable differences are observed, like signal accentuation in borders. For example, in the water component estimated with IDEAL, an intensified signal band can be observed. Also, due to the lower noise of FIRST estimates, more details can be appreciated in fat images (lower arrow). All images are shown with the same intensity scale.

$R_2^*$  estimation specially difficult. Although a smoothing for  $R_2^*$  is not specified in the original literature of IDEAL, this step is included to address the high variance present in the  $R_2^*$  map, which leads to noisy species estimates. Brain images can be found in Figs. 5–7. Brain acquisitions at the orbits level are particularly difficult in water–fat separation procedures due to the high field inhomogeneities caused by the air present in the sinus, as Fig. 6 shows. High field inhomogeneities could cause high frequency fat–water swapping, degrading the quality of the species estimates. Nevertheless, high frequency field variations were not observed throughout the image when using both methods. These variations are attenuated in IDEAL because the field map is smoothed in the final step, which yields a less defined field map. It is important to note that the field inhomogeneity and  $R_2^*$  estimates of FIRST remain very

close to the starting point in areas where there is no signal. In practice, estimates of these variables with low noise backgrounds improve the visualization of the generated maps. Low changes in the maps can be understood by looking at the gradients of the objective function (Appendix B), where the change of the estimates of field inhomogeneity and  $R_2^*$  are directly weighed by the object intensities. Good estimates for  $R_2^*$  maps were obtained with FIRST and IDEAL considering only four echoes. Results for the phantom study are shown in Fig. 8. The line profile shows successful fat displacement correction with FIRST. In the center region, where the oil tube is present, a fat fraction of nearly 15% is obtained with both estimation methods. Both algorithms successfully achieve water–fat separation in this area, while image-space displacements are corrected when using a  $k$ -space approach.

FIG. 3. For the thigh, left and right images show the calculated field inhomogeneity map with IDEAL and FIRST, respectively. The field map calculated with IDEAL was smoothed with a  $5 \times 5$  and  $\sigma = 1.5$  gaussian filter, while FIRST was not smoothed at all. Similar intensities are observed for both methods, validating our technique for the measurement of the field map. An advantage of FIRST is given by the small changes of the complex field map where the signal level is low. This results in reduced background noise.





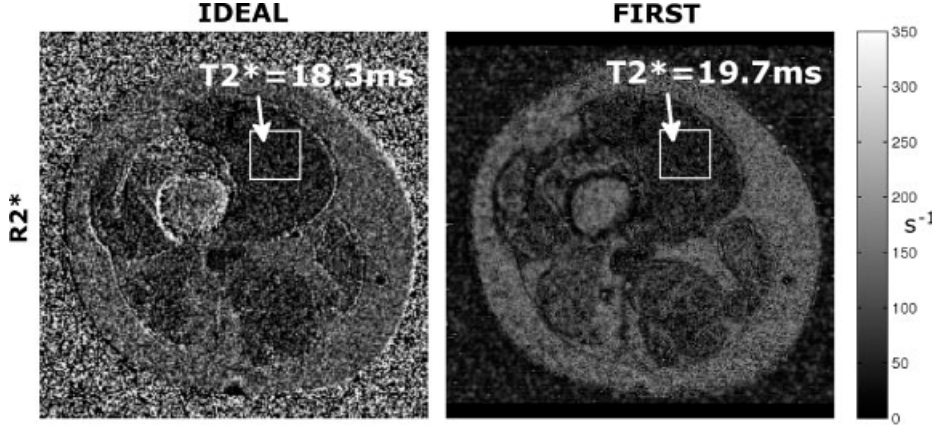


FIG. 4. For the thigh, left and right columns show the calculated  $R_2^*$  maps with IDEAL and FIRST, respectively. The  $R_2^*$  map of IDEAL was smoothed with a  $5 \times 5$  and  $\sigma = 0.5$  gaussian filter, as explained in First Algorithm section. The shown  $T_2^*$  values were calculated as the mean of a  $20 \times 20$  rectangle. This area is delimited by a white rectangle, pointed by the arrows. In this case, we can see a lower value of  $T_2^*$  with IDEAL, yielding higher signal intensities when compared to FIRST. A smoother map is obtained with FIRST, avoiding peak values which may lead to incorrect estimation of  $R_2^*$ .

To study the effects of the presence of noise in the measured data, we reconstructed several times the data from the phantom adding noise at the input. It was observed that the root mean square error (RMSE) is approximately the same for both techniques. For example, in the area indicated in Fig. 8 this value was 0.564% for IDEAL and 0.696% for FIRST. As a definition of RMSE, the following expression was used  $\sqrt{\sum_t \sum_n |f_{n,t} - f_0|^2 / NT}$  where  $f_{n,t}$  is the pixel value at position  $n$  and reconstruction  $t$ , considering a set of  $N$  pixels and  $T$  different reconstructions. The  $f_0$  value was computed as the average of the composite image obtained with IDEAL. Therefore, when calculating the RMSE it is assumed that the actual intensity is constant in that region. These computations were performed

on the composite image (complex sum of water and fat). The RMSE percentage values indicated were calculated with respect to  $f_0$ . The procedure was repeated 50 times using the same acquisitions detailed in the Materials and Methods section, using a  $20 \times 3$  pixels rectangle.

## DISCUSSION

Our frequency space-based approach calculates simultaneously estimates of species, field inhomogeneity, and  $R_2^*$  maps. By calculating the field and  $R_2^*$  maps concurrently with the species, we obtain nonshifted estimates of the first two. Additionally, the proposed method corrects image-space displacement of species due to chemical

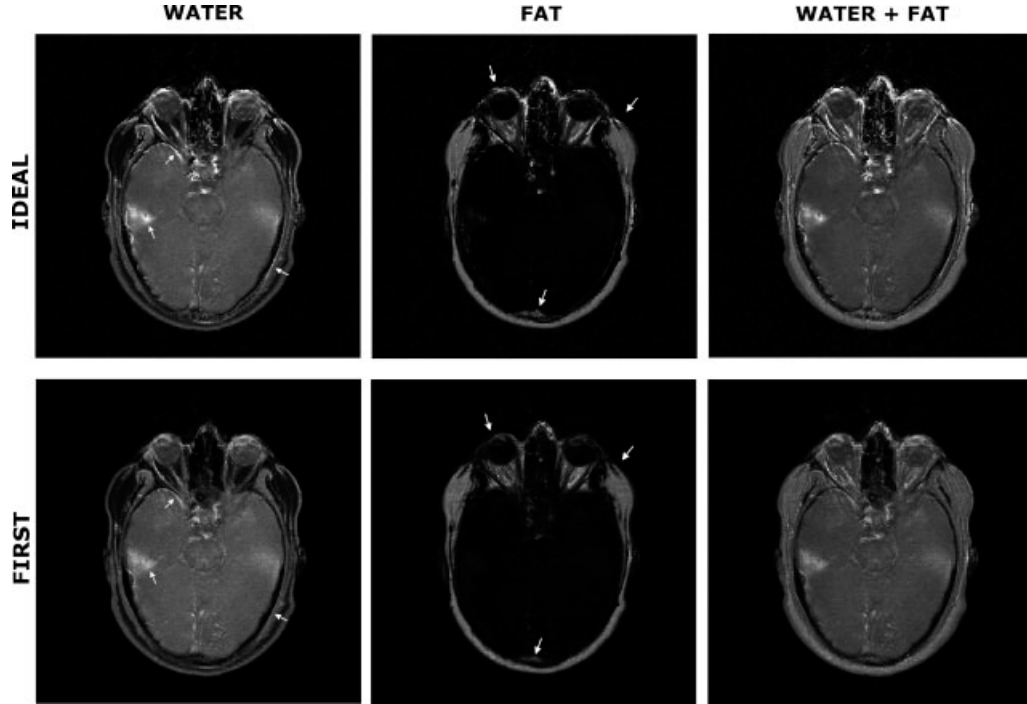
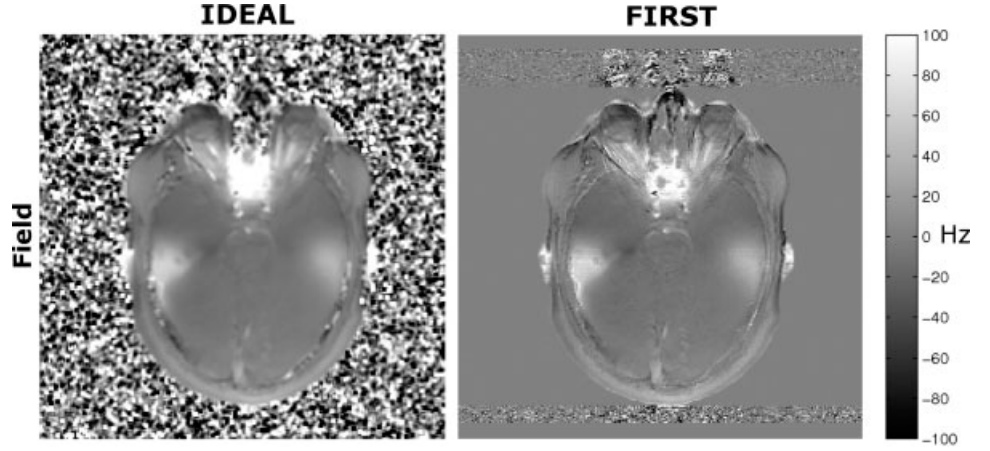


FIG. 5. Magnitude images of water, fat and complex sum of both components for the brain. The upper and lower rows show the results for IDEAL and FIRST, respectively. Lower noise is observed for both separation methods when compared to thigh experiments, due to the larger voxel size of the input images. Higher signal intensities are observed for the water and fat estimates of IDEAL, shown by the arrows. All images are shown with the same intensity scale.

FIG. 6. For brain imaging, calculated field inhomogeneity map with IDEAL and FIRST. The field map calculated with IDEAL was smoothed with a  $5 \times 5$  and  $\sigma = 1.5$  gaussian filter. For both algorithms, phase wrap is observed near the sinus, a region of high field inhomogeneity.



shift and field inhomogeneity (Figs. 2–7). As shown in the results, this technique achieves accurate and reliable water–fat separation. Structures that may remain hidden are easily distinguished with our method. Besides, a smoother  $R_2^*$  map is generated with FIRST, avoiding peak intensities which may lead to erroneous calculation of this parameter.

We have shown that the water signal calculated with image space-based algorithms is erroneously intensified in areas where there is water–fat overlap due to chemical shift artifacts (Figs. 2 and 5). Techniques using variable time maps with pre-separation  $R_2^*$ -correction also suffer from this problem, because the  $R_2^*$  map is estimated before off-resonance correction, obtaining a shifted estimate of the  $R_2^*$  map. This artifact is repaired when adopting a simultaneous estimation scheme like the one we have presented. In the case where different bandwidths are needed for each echo, each acquisition will suffer from different off-resonance artifacts in image space, leading to erroneous estimation of the field inhomogeneity and  $R_2^*$  maps if these are calculated from the input images. Although it was not evaluated, our method would allow different bandwidth acquisitions, without sacrificing accuracy in the estimation of the field and  $R_2^*$  maps.

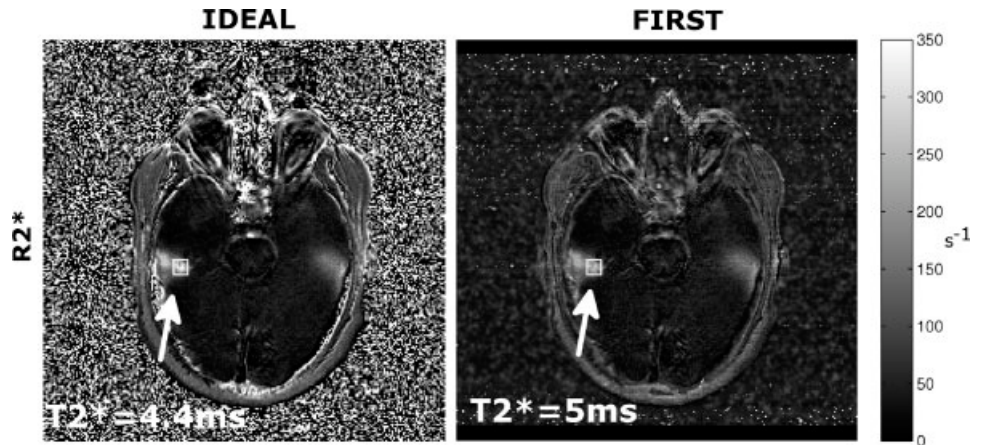
As has been already noted, the water–fat separation problem has multiple solutions if the field inhomogeneity is not bounded to an adequate range. This range depends on the

resonant frequencies of the species (3,6,9,22). Therefore, the optimization problem proposed in Eq. 1 is nonconvex. A priori, interior-point algorithms are not well-suited for nonconvex problems, where several local minima coexist (27,28), and the global minima can be obtained with multiple solutions. In our case, the algorithm is capable of generating a reasonable solution due to the chosen starting points and the boundaries for the unknown variables. In fact, using only bounds and no other type of restrictions simplify significantly the calculation of the logarithmic barrier of the interior-point method. For FIRST, the starting point of species and field map is chosen to be zero. For the  $R_2^*$  map, an exponential fitting of the magnitude values of the acquired images is used as initial value, which results in faster convergence to the solution. Because of the characteristics of the chosen algorithm, it is important to broaden the bounds of the variables, because interior-point method solutions never lie totally in the specified boundaries (30).

Our final implementation for solving the minimization problem consisted of two steps. Empirically, we found that separating into two steps was faster than solving the whole problem at once. The objective function value obtained when solving the minimization problem in a single step was 10% higher than the value obtained with two steps for equal processing time.

An important problem in species separation techniques is water–fat swap. Different heuristics can be included to

FIG. 7. For brain imaging, calculated  $R_2^*$  maps with IDEAL and FIRST. The  $R_2^*$  maps were not smoothed except for the starting point, as explained in First Algorithm section. The shown  $T_2^*$  values were calculated as the mean of an  $8 \times 8$  rectangle. This area is delimited by a white rectangle, pointed by the arrows. Similar to thigh imaging, IDEAL estimates a shorter  $T_2^*$  time when compared to FIRST, which yields higher intensity values. This can cause over-estimation of the fat fraction.



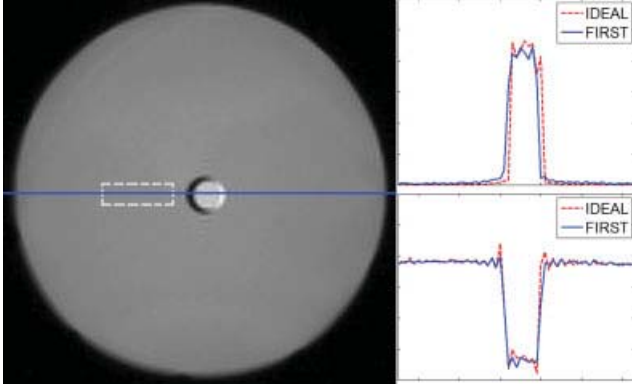


FIG. 8. Using a home-made phantom consisting of an oil tube surrounded by water, the performance of FIRST and IDEAL was studied in areas of hard water-fat transitions and noticeable presence of both fat and water. A profile for fat (top) and water (bottom) estimates calculated with FIRST (continuous line) and IDEAL (dashed line) is shown, demonstrating the advantages of FIRST for correcting image displacements due to chemical shift. Both algorithms behave correctly when fat and water are present in the same pixel. The profiles are shown in the same scale. The area delimited by the dashed rectangle in the image was used to calculate the RMSE values presented in the Results section.

avoid rapidly changing field map estimates. Given our theoretical framework, it is convenient to include field map smoothness restrictions in the optimization problem. Several smoothness conditions have been proposed to address this issue (22,31,32). On the other hand, some image-space techniques have been proposed for species separation in the presence of high field inhomogeneities, such as region growing methods for field map estimation (33).

FIRST was demonstrated with datasets with traditional Cartesian spin warp, but our theoretical framework allows any  $k$ -space trajectory, and even different trajectories for each echo. A specific implementation that takes advantage of the time map characteristics of Cartesian spin warp was implemented, and a more general computational solver for any 2D sequence is being explored as future work. With a general 2D solver, radial, spiral and other trajectories can be used in combination with our method.

Multipeak fat spectrum modeling has proved to be useful for fat separation techniques. A multipeak model can be easily incorporated to our approach. The amplitude coefficients and peak frequencies of the fat spectrum can be calculated on a patient-specific basis through spectroscopy or other method.

The main limitations of this work can be summarized in two. The first one is computational time for separation. For datasets of the same size, FIRST takes 71 min, much longer than the 9 min of  $T_2^*$ -IDEAL. Choosing a more suitable optimization algorithm for this kind of nonlinear problem is being studied as an option. The variable projection method (34,35) has been previously used in MRI and MR spectroscopy for species separation purposes with promising results (8,36). This approach will be studied for the application to the proposed theory. The second limitation is that a single  $R_2^*$  value is assumed for both species, which leads to suboptimal fat quantification (17). Anyhow, this issue can be addressed with our proposed scheme,

without increasing the number of variables required for solving the fat-water separation problem. We have adopted a solution that in a first step the field map is calculated along with the species, leaving a set of  $N$  redundant equations. If in the second step the field map from the previous step is considered correct, therefore calculating only the  $R_2^*$  map and the species, we leave  $N$  free equations. This set of free equations can be used for calculating independent  $R_2^*$  values for fat and water. An approach for calculating two different  $R_2^*$  values with IDEAL has been presented recently in Ref. 37. This feature is being considered for future implementations.

In summary, a method for simultaneously estimating chemical species, field inhomogeneity, and  $T_2^*$  maps without off-resonance displacements was presented, obtaining excellent results in different anatomies.

## APPENDIX A

### Formulation for 2D Cartesian Acquisitions

Extending the formulation of FIRST Signal Model section to a 2D acquisition, the signal for one specific TE can be described as

$$\begin{aligned} S(k_x, k_y) &= \sum_{m=1}^M \iint \rho_m(x, y) \\ &\quad \times e^{-i2\pi(xk_x + yk_y + (\Delta f_m + \psi(x, y)) \cdot t)} dx dy \\ &= \sum_{m=1}^M \int \left( \int \rho_m(x, y) \right. \\ &\quad \times \left. e^{-i2\pi(xk_x + (\Delta f_m + \psi(x, y)) \cdot t)} dx \right) e^{-i2\pi y k_y} dy \quad [A1] \end{aligned}$$

where the readout time  $t$  for an echo  $n$  can be described as  $t = TE_n + \tau_n = TE_n + \alpha_n k_x$ , with  $\tau_n$  the time between each sampling time and the TE of the acquisition. Assuming the same time map for each  $k$ -space line (such as in cartesian acquisitions) and applying an inverse Fourier transform in the “ $y$ ” direction to A1,

$$\begin{aligned} g(k_x, y') &= \mathcal{F}_y^{-1}\{S(k_x, k_y)\} = \int S(k_x, k_y) e^{i2\pi k_y y'} dk_y \\ &= \sum_{m=1}^M \iiint \rho_m(x, y) e^{-i2\pi(xk_x + (\Delta f_m + \psi(x, y)) \cdot (TE + \alpha k_x))} \\ &\quad \times e^{-i2\pi y k_y} e^{i2\pi k_y y'} dx dy dk_y \\ &= \sum_{m=1}^M \iint \rho_m(x, y) e^{-i2\pi(xk_x + (\Delta f_m + \psi(x, y)) \cdot (TE + \alpha k_x))} \\ &\quad \times \left( \int e^{-i2\pi(y - y') k_y} dk_y \right) dx dy \\ &= \sum_{m=1}^M \iint \rho_m(x, y) e^{-i2\pi(xk_x + (\Delta f_m + \psi(x, y)) \cdot (TE + \alpha k_x))} \\ &\quad \times \delta(y - y') dx dy \\ &= \sum_{m=1}^M \int \rho_m(x, y') e^{-i2\pi(xk_x + (\Delta f_m + \psi(x, y')) \cdot (TE + \alpha k_x))} dx \end{aligned}$$



which leads to a much simpler 1D optimization in a row by row basis. The objective function described in Eq. 1 can be used for every row.

## APPENDIX B

### Gradients of the Objective Function

For each optimization variable, the gradient function was explicitly calculated. If  $S^a$  and  $S^e$  correspond to the acquired and estimated signals, respectively, the gradient of the objective function  $f$  toward a Certain variable  $v$  is the following:

$$\begin{aligned}\frac{\partial f}{\partial v} &= \frac{\partial}{\partial v} \|S^a - S^e\|^2 \\ &= 2 \cdot \frac{\partial}{\partial v} (S^a - S^e) \cdot (S^a - S^e)^* \\ &= -2 \cdot \left( (S^a - S^e) \cdot \frac{\partial S^{e*}}{\partial v} + (S^a - S^e)^* \cdot \frac{\partial S^e}{\partial v} \right).\end{aligned}$$

The partial derivatives for each variable are

$$\begin{aligned}\frac{\partial S^e}{\partial \rho_{m,r}} &= e^{-i2\pi((\Delta f_m + \tilde{\psi}_r) \cdot q + r k_q)} \\ \frac{\partial S^e}{\partial \psi_r} &= -i2\pi q \sum_{m=1}^M \rho_{m,r} e^{-i2\pi((\Delta f_m + \tilde{\psi}_r) \cdot q + r k_q)} \\ \frac{\partial S^e}{\partial R_{2,r}} &= -q \cdot \sum_{m=1}^M \rho_{m,r} e^{-i2\pi((\Delta f_m + \tilde{\psi}_r) \cdot q + r k_q)}.\end{aligned}$$

All these results are within a single acquisition.

## REFERENCES

- Hussain HK, Chenevert TL, Londy FJ, Gulani V, Swanson SD, McKenna BJ, Appelman HD, Adusumilli S, Greenson JK, Conjeevaram HS. Hepatic fat fraction: MR imaging for quantitative measurement and display—early experience. *Radiology* 2005;237:1048–1055.
- Bley T, Wieben O, Francois CJ, Brittain JH, Reeder SB. Fat and water magnetic resonance imaging. *J Magn Reson Imaging* 2010;31:4–18.
- Dixon WT. Simple proton spectroscopic imaging. *Radiology* 1984;153:189–194.
- Glover GH, Schneider E. Three-point Dixon technique for true water/fat decomposition with  $B_0$  inhomogeneity correction. *Magn Reson Med* 1991;18:371–383.
- Glover GH. Multipoint Dixon technique for water and fat proton and susceptibility imaging. *J Magn Reson Imaging* 1991;1:512–530.
- Skinner TE, Glover GH. An extended two-point Dixon algorithm for calculating separate water, fat, and  $B_0$  images. *Magn Reson Med* 1997;37:628–630.
- Coombs BD, Szumowski J, Coshaw W. Two-point Dixon technique for water–fat signal decomposition with  $B_0$  inhomogeneity correction. *Magn Reson Med* 1997;38:884–889.
- Hernando D, Halder JP, Sutton BP, Ma J, Kellman P, Liang ZP. Joint estimation of water/fat images and field inhomogeneity map. *Magn Reson Med* 2008;59:571–580.
- Reeder SB, Wen Z, Yu H, Pineda AR, Gold GE, Markl M, Pelc NJ. Multicoil Dixon chemical species separation with an iterative least-squares estimation method. *Magn Reson Med* 2004;51:35–45.
- Reeder SB, McKenzie CA, Pineda AR, Yu H, Shimakawa A, Brau AC, Hargreaves BA, Gold GE, Brittain JH. Water–fat separation with IDEAL gradient-echo imaging. *Magn Reson Med* 2007;25:644–652.
- Kim H, Taksali SE, Dufour S, Befroy D, Goodman TR, Petersen KF, Shulman GI, Caprio S, Constable RT. Comparative MR study of hepatic fat quantification using single-voxel proton spectroscopy, two-point dixon and three-point IDEAL. *Magn Reson Med* 2008;59:521–527.
- Jenkinson M. Fast, automated, N-dimensional phase-unwrapping algorithm. *Magn Reson Med* 2003;49:193–197.
- Hernando D, Kellman P, Halder JP, Liang ZP. Robust water/fat separation in the presence of large field inhomogeneities using a graph cut algorithm. *Magn Reson Med* 2010;63:79–90.
- Guio B, Aho S. Quantification of liver fat content : Comparison of triple-echo and in vivo proton MR spectroscopy 1. *Clin Res* 2009;250:95–102.
- Hamilton G, Middleton MS, Bydder M, Yokoo T, Schwimmer JB, Kono Y, Patton HM, Lavine JE, Sirlin CB. Effect of PRESS and STEAM sequences on magnetic resonance spectroscopic liver fat quantification. *J Magn Reson Imaging* 2009;30:145–152.
- Bydder M, Yokoo T, Hamilton G, Middleton MS, Chavez AD, Schwimmer JB, Lavine JE, Sirlin CB. Relaxation effects in the quantification of fat using gradient echo imaging. *Magn Reson Imaging* 2008;26:347–359.
- Chebrolov VV, Hines CDG, Yu H, Pineda AR, Shimakawa A, McKenzie CA, Samsonov A, Brittain JH, Reeder SB. Independent estimation of  $T_2^*$  for water and fat for improved accuracy of fat quantification. *Magn Reson Med* 2010;63:849–857.
- Wood JC, Enriquez C, Ghugre N, Tyzka JM, Carson S, Nelson MD, Coates TD. MRI  $R_2$  and  $R_2^*$  mapping accurately estimates hepatic iron concentration in transfusion-dependent thalassemia and sickle cell disease patients. *Blood* 2005;106:1460–1465.
- Yu H, McKenzie CA, Shimakawa A, Vu AT, Brau AC, Beatty PJ, Pineda AR, Brittain JH, Reeder SB. Multiecho reconstruction for simultaneous water–fat decomposition and  $T_2^*$  estimation. *J Magn Reson Imaging* 2007;26:1153–1161.
- Wang K, Yu H, Brittain JH, Reeder SB, Du J. k-space water-fat decomposition with  $T_2^*$  estimation and multifrequency fat spectrum modeling for ultrashort echo time imaging. *J Magn Reson Imaging* 2010;31:1027–1037.
- Machann J, Thamer C, Schnoedt B, Stefan N, Haring HU, Claussen CD, Fritsche A, Schick F. Hepatic lipid accumulation in healthy subjects: a comparative study using spectral fat-selective MRI and volume-localized 1H-MR spectroscopy. *Magn Reson Med* 2006;55:913–917.
- Hernando D, Liang ZP, Kellman P. Chemical shift-based water/fat separation: a comparison of signal models. *Magn Reson Med* 2010;64:811–822.
- Brotsky EK, Chebrolov VV, Block WF, Reeder SB. Frequency response of multipoint chemical shift-based spectral decomposition. *J Magn Reson Imaging* 2010;32:943–952.
- Eggers H, Boernert P, Koken P. Spiral water-fat imaging with integrated off-resonance correction on a clinical scanner. In: *Proc Intl Soc Mag Reson Med*, *J Magn Reson Imaging*, vol. 19. 2011. p 752.
- Brotsky EK, Holmes JH, Yu H, Reeder SB. Generalized k-space decomposition with chemical shift correction for non-Cartesian water–fat imaging. *Magn Reson Med* 2008;59:1151–1164.
- Pineda AR, Reeder SB, Wen Z, Pelc NJ. Cramér-Rao bounds for three-point decomposition of water and fat. *Magn Reson Med* 2005;54:625–635.
- Karmarkar N. A new polynomial-time algorithm for linear programming. *Combinatorica* 1984;4:373–395.
- Byrd RH, Hribar ME, Nocedal J. An interior point algorithm for large-scale nonlinear programming. *SIAM J Optim* 1999;9:877–900.
- Gatehouse P, Bydder G. Magnetic resonance imaging of short  $T_2$  components in tissue. *Clin Radiol* 2003;58:1–19.
- Nocedal J, Wright SJ. Numerical optimization. New York: Springer-Verlag; 1999.
- Samsonov A, Fessler J, Huh W. Water–Fat decomposition with regularized field map. In: *Proc Intl Soc Mag Reson Med*, Toronto, vol. 16. 2008. p. 1382.
- Funai AK, Fessler JA, Yeo DTB, Olafsson VT, Noll DC. Regularized field map estimation in MRI. *IEEE Trans Med Imaging* 2008;27:1484–1494.
- Yu H, Reeder SB, Shimakawa A, Brittain JH, Pelc NJ. Field map estimation with a region growing scheme for iterative 3-point water–fat decomposition. *Magn Reson Med* 2005;54:1032–1039.
- Golub G, Pereyra V. The differentiation of pseudoinverses and nonlinear least squares problems whose variables separate. *SIAM J Numer Anal* 1972;10:413–432.
- Golub G, Pereyra V. Separable nonlinear least squares: the variable projection method and its applications. *Inverse Probl* 2003;19:R1–R26.
- van der Veen JW, de Beer R, Luyten PR, van Ormondt D. Accurate quantification of in vivo  $^{31}\text{P}$  NMR signals using the variable projection method and prior knowledge. *Magn Reson Med* 1988;6:92–98.
- Janiczek RL, Gambarota G, Sinclair CDJ, Yousry Ta, Thornton JS, Golay X, Newbould RD. Simultaneous  $T_2$  and lipid quantitation using IDEAL-CPMG. *Magn Reson Med* in press.